ELSEVIER

Stable bismuth-antimony alloy cathode with a conversion-dissolution/deposition mechanism for high-performance zinc batteries

Yuwei Zhao [1], Feng Jiang [2], Hu Hong [1], Donghong Wang [3], Qing Li [1], You Meng [1], Zhaodong Huang [1], Ying Guo [1], Xinliang Li [1], Ao Chen [1], Rong Zhang [1], Shaoce Zhang [1], Johnny C. Ho [1], Zhenpeng Yao [4,*], Weishu Liu [2,*], Chunyi Zhi [1,3,*]

[1] Department of Materials Science and Engineering, City University of Hong Kong, Hong Kong, China
[2] Department of Materials Science and Engineering, Southern University of Science and Technology, Shenzhen, China
[3] Hong Kong Center for Cerebro-Cardiovascular Health Engineering (COCHE), Shatin, NT, Hong Kong, China
[4] Department of Materials Science and Engineering, Shanghai Jiao Tong University, Shanghai, China

Although a large number of intercalation cathode materials for aqueous Zn batteries have been reported, limited intercalation capacity precludes achieving a higher energy density. Here we develop a high-performance aqueous Zn battery based on BiSb alloy ($Bi_{0.5}Sb_{0.5}$) using a high-concentrated strong-basic polyelectrolyte. We demonstrate that a conversion-dissolution/deposition electrochemical mechanism ($BiSb \leftrightarrow Bi + SbO_2^- \leftrightarrow Bi + SbO_3^- \leftrightarrow Bi_2O_3$) through in situ X-ray diffraction (XRD), Raman, and ex-situ X-ray photoelectron spectrometry (XPS) characterizations with the help of density functional theory calculations. The BiSb cathode delivers large capacity of 512 mAh g^{-1} at 0.3 Ag^{-1} and superior rate capability of 90 mAh g^{-1} even at 20 Ag^{-1}, and long-term cyclability with capacity retentions of 184 mAh g^{-1} after 600 cycles at 0.5 Ag^{-1} and 130 mAh g^{-1} after 1300 cycles at 1 Ag^{-1}. Remarkably, even at temperatures as low as −10 and −20 °C, capacities of 210 and 197 mAh g^{-1} are reserved at 1 Ag^{-1}, respectively. Moreover, the prepared pouch Zn//BiSb battery delivers a high energy density of 303 Wh kg_{BiSb}^{-1} at 0.3 Ag^{-1}. When coupled with a high concentration polyelectrolyte, the Zn/BiSb battery exhibits an excellent performance over a wide temperature range (−40 to 40 °C). Our research reveals the metal cathode is promising for Zn batteries to achieve a high performance with the unique mechanism and alloys can be an effective approach to stabilize metal electrodes for cycling.

Keywords: Zinc batteries; Bismuth-antimony alloy; Conversion reaction; Low temperature battery

Introduction

The rechargeable zinc batteries (RZBs), as an alternative power solution to lithium ion batteries (LIBs), have received increasing interest recently due to their advantages of low cost, good safety, and excellent electrochemical performance (high theoretical capacity of 820 mAh g^{-1} or 5854 mAh cm^{-3} based on Zn anode) [1,2]. So far, a variety of RZBs operated under neutral, alkaline, and acid conditions were reported. Cathode material of the RZBs is a major constraint for zinc storage capacity, which currently covers a wide range materials, such as Prussian blue analogs [3–5], transition metal oxides/dichalcogenides (Mn, V, Co, Mo, Ni or Ag-based compound) [6], organics [7], polyanion and so on [8]. Most of these cathode materials employ an intercalation mechanism, which results in a limited capacity and precludes achieving a high energy density due to the electrode kinetic properties are poor because of the larger ionic radius and valence

* Corresponding authors.
E-mail addresses: Yao, Z. (yaozhenpeng@gmail.com), Liu, W. (liuws@sustech.edu.cn), Zhi, C. (cy.zhi@cityu.edu.hk).

 https://doi.org/10.1016/j.mattod.2021.09.023

state of Zn^{2+} compared with Li^+ and Na^+ [9,10]. Cathode materials that can undergo multi-electron conversion/alloying reactions are highly expected.

Metal-based materials including metals (Ge [11], Sn [12], Bi [13], Sb [14], Pb, etc.) and alloys [15] feature earth abundance and high theoretical capacities (300–2000 mAh g^{-1}) in the employments in LIBs, sodium-ion batteries, and potassium ion batteries. Metal based cathodes may undergo multi-electron conversion/alloying reactions, which may potentially provide a high capacity. However, they may experience large volume change during cycling, leading to a poor stability. However, the research on zinc storage in metal-based materials is still in its infancy stage and faces a serious challenge. The main problem of zinc storage in metal-based materials is the huge volume expansion leading to severe capacity fading. To solve the issue, effective strategies including hierarchy structure designation [1,16], preparing carbon-based composites [4,17], and alloying [18,19] are developed in Li/Na/K-ion batteries. Nevertheless, further research is needed to simplify the preparation process, improve repeatability, and reduce cost especially for mass production, so that the nanostructures fabrication can be realized in large-scale production. Mixing with carbon materials also faces the problem of insufficient specific capacity. Alloying is an important approach to provide an effective buffering to volume fluctuation of metal electrode. Hence it is vital to study the electrochemical behavior of alloys with different compositions to activate both high capacity and superior cycling stability in RZBs.

Bismuth-antimony (Bi-Sb) alloys are very promising bimetallic alloys for electrochemical energy storage due to the following advantages: (1) Bi and Sb serve as each other's buffer substrate to effectively restrain the volume change [20]. (2) The two high-performance active metal elements ensure high capacity. (3) Given the same main group of Bi and Sb, their similar physiochemical properties ensure flat potential plateaus and flexibility in compositional ratio design ($Bi_{1-x}Sb_x$, $0 < x < 1$) [21]. (4) High electrical conductivity of Sb (2.56×10^6 S·m^{-1}) facilitates a potentially excellent rate capability [20,22]. However, the promising alloy electrode has not yet been investigated in RZBs. Apart from the alloy electrode with superb performance, the electrolyte is also the key for stabilization of electrode structures and enhancement of electrochemical performance due to the interface chemical reaction [23].

Herein, for the first time the BiSb alloy ($Bi_{0.5}Sb_{0.5}$) is prepared via a facile high-energy mechanical milling method and used as cathodes of RZBs using a high concentration polyelectrolyte (sodium polyacrylate (PANa) hydrogel soaked with 0.3 M Zn $(Ac)_2$ and 6 M KOH). In these components, the BiSb cathode delivers a large capacity of 512 mAh g^{-1} at 0.3 Ag^{-1} and 90 mAh g^{-1} even at a high rate of 20 Ag^{-1}, and the best cycling performance with capacity retentions of 184 mAh g^{-1} after 600 cycles at 0.5 Ag^{-1} and 130 mAh g^{-1} after 1300 cycles at 1 Ag^{-1} in sharp contrast to the rapid capacity decay of the pure Bi cathode and the limited capacity of the Sb cathode. We elucidate a conversion-dissolution/deposition electrochemical mechanism ($BiSb \leftrightarrow Bi + SbO_2^- \leftrightarrow Bi + SbO_3^- \leftrightarrow Bi_2O_3$) through in-situ XRD, Raman, and ex-situ XPS analysis assisted with density functional theory (DFT) calculations. The synergy of the BiSb cathode with high conductivity, stable structure, unique reaction mechanism and high concentration polyelectrolyte enable excellent performance over a wide temperature range.

The crystal structures of BiSb alloy, Bi and Sb metals are studied by X-ray diffraction (XRD) patterns, as shown in Fig. 1a. All these patterns show similar characteristic reflections and pure polycrystalline phases indexed to the trigonal phase (Bi: JCPDS. 44-1246; BiSb: JCPDS no. 35-0517; Sb: JCPDS no. 35-0732). With the addition of smaller Sb atoms in the Bi crystal structure, the reflections of BiSb shift to higher 2θ values, which confirms the decrease of lattice constants conforming to the Vegard's law. The Rietveld-refined XRD pattern of BiSb, and calculated crystal structure and lattice parameters are shown in Fig. 1b, c, and Fig. S1, respectively. Annular dark field-scanning transmission electron microscopy (ADF-STEM) is employed to analyze the microstructure and morphology of BiSb (Fig. 1d). BiSb nanoparticles in the range 1–100 nm are uniformly distributed in an amorphous matrix, which is SbO_x and Bi_2O_3 amorphous oxide layer formed during the mechanical milling process. These matrices hold the role of ensuring the BiSb tightly connected to the conductive agent, potentially stabilizing the BiSb particles during charge/discharge processes [24]. The illustration in Fig. 1d shows the selected-area electron diffraction (SAED) pattern attributed to the BiSb manifesting the nature of nanocrystalline. Moreover, Fig. 1e and f and Fig. S2 show high-resolution transmission electron microscopy (HRTEM) images revealing that the crystalline BiSb nanoparticles with lattice fringes of the (003), and (012) crystal planes are wrapped in the amorphous substrate. The corresponding diffraction spots of BiSb are also visible in the SAED/-fast Fourier transform (FFT) patterns. Energy-dispersive spectroscopy (EDS) mappings also display a uniform distribution of Bi, and Sb elements (Fig. 1g).

Next, the electrochemical performances of BiSb alloy are evaluated as cathodes of a RZB using the quasi-solid PANa hydrogel electrolyte with 0.3 M $Zn(Ac)_2$ and 6 M KOH. Fig. 2a shows cyclic voltammogram (CV) behaviors of the Zn//BiSb battery at 1 mV/s. Metal Bi and Sb cathodes have one (0.75 V) and two (0.43/0.33 V) obvious reduction peaks, respectively. In contrast, BiSb shows three pairs of redox peaks and the strongest reduction peak at 0.71 V. The galvanostatic charge/discharge (GCD) curves at 0.8 A/g of BiSb alloy, Bi and Sb are also compared in Fig. 2b. Sb delivers short ramp plateaus and a limited specific capacity of 150 mAh g^{-1}. Metal Bi cathode exhibits a very flat discharge plateau at around 0.76 V and a specific capacity of 240.3 mAh g^{-1} at 0.8 A/g. Compared with the discharge plateau of Bi, the other two plateaus emerging from Sb located at 0.49 and 0.42 V are observed for the BiSb cathode offering the highest specific capacity of 311 mAh g^{-1} at 0.8 A/g. Fig. 2c and Fig. S3 exhibit CV curves of the Bi_xSb_{1-x} alloys, Bi and Sb tested at various scan rates. With the increase of the scan rate, the oxidation peaks of BiSb shift to a higher voltage, while the reduction peaks move to a lower voltage gradually. The three pairs of redox peaks of BiSb are located at 0.72/0.97 V, 0.48/0.83 V, and 0.43/0.65 V, respectively. Further studies of the rate capabilities of BiSb are shown in Fig. 2d. Impressively, the BiSb shows excellent rate capability with specific capacities of 465, 361, 300, 257, 192, 141, 102, and ~94 mAh/g at 0.3, 0.5, 0.8, 1, 2, 3, 5, and 10–20 A/g, respectively. However, Bi has discharge capacities of only 353 and 44 mAh/g

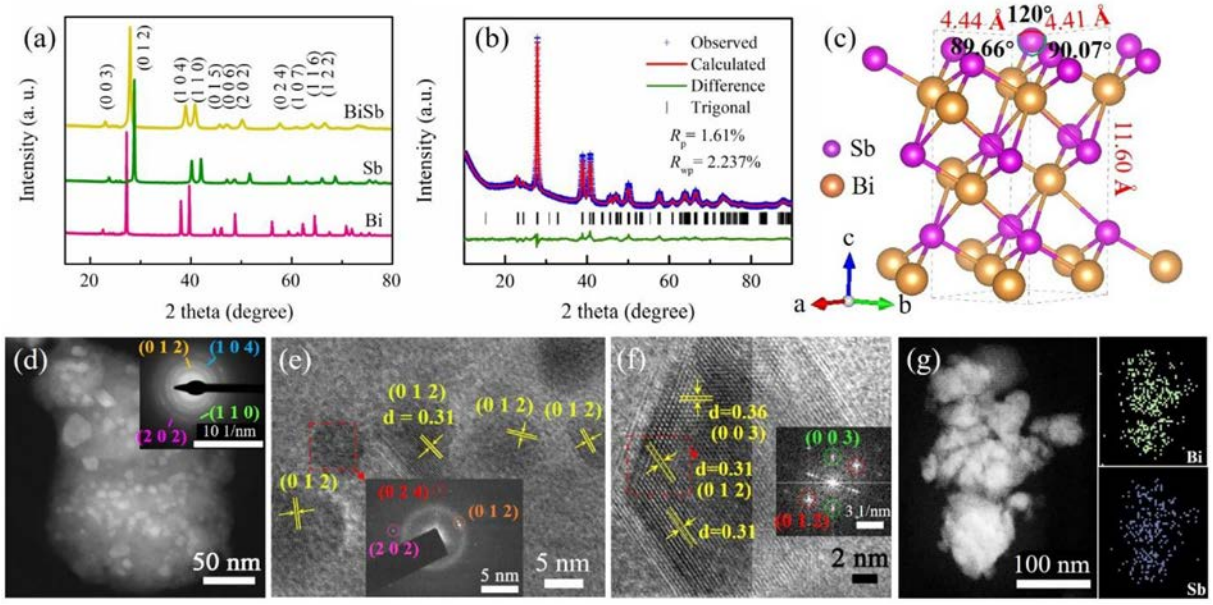

FIGURE 1

Structure, morphology, and conductivity analyses of the prepared BiSb alloy. (a) XRD patterns of BiSb alloy, Bi, and Sb powders. (b) Rietveld analysis of the XRD pattern of BiSb powders and (c) the corresponding crystal structure labeled with the lattice parameters. (d) ADF-STEM image of BiSb with an inset showing SAED pattern. (e and f) HRTEM images and corresponding SAED and FFT patterns of the BiSb sample. The contrast of left and right part of (f) is due to a special camera of the TEM. (g) EDS mappings of the BiSb sample.

at 0.3 and 20 A/g, respectively (Fig. S4a). The corresponding discharge/charge profiles of BiSb and Bi are displayed in Fig. 2e and Fig. S4b, respectively. Then, we compare the performance of our batteries with the reported common aqueous RZBs (Fig. 2f). Zn//BiSb exhibits both high specific power (1235 W kg^{-1}_{BiSb}) and high specific energy (560 Wh kg^{-1}_{BiSb}) in comparison with representative Mn, V-based cathodes, and Prussian blue analogs in RZBs [5,25]. Furthermore, the cycle performances of Bi, Sb and Bi_xSb_{1-x} alloys are evaluated in Fig. 2g and Fig. S5. BiSb delivers the highest capacities and optimal cycling of 183 mAh g^{-1} after 600 cycles at 0.5 A/g. BiSb also exhibits 130 mAh g^{-1} after 1300 cycles at 1 A/g with the Columbic efficiency (CE) of around 100% except the low initial CEs. Other alloys show much higher CE at the end of the cycle, indicating that the side reaction of the electrode is the main reason for the failure of the battery. Particularly the capacity of Bi increases at first and then decreases sharply during cycling, and finally the Bi cathode shows poor electrical contact caused by the dramatic volume expansions during the charge/discharge process. These results show that BiSb enables the cells to keep stable cycles and obtain high capacities. When compared with other Bi, Sb-based batteries (Fig. 2h), the superior cyclic stability (130 mAh g^{-1} after 1300 cycles) can rival almost all of them even they are mostly based on organic electrolyte [26]. In comparison with metal cathode in alkaline aqueous batteries including Zn//Co, Zn//Bi, Zn//Ni, Zn//Cu and Zn//Ag, Zn//BiSb also shows a much better stability (Fig. S6).

The surface morphologies of Bi and BiSb cathodes during cycling are investigated. Fig. 3a–c and Fig. 3d–f show the evolution of Bi and BiSb morphology after 50, 100, and 150 cycles, respectively. Fig. S7 shows the surface topography of the initial Bi and BiSb cathodes. As the cycle progresses, Bi particles on the cathode surface become crushing and unevenly distributed and the cathode surface gets rougher and rougher (Fig. 3a–c). In striking contrast, BiSb particles are uniformly distributed on the cathode surface during the cycle and there is no significant change in the particle size sustaining the flat and integrity surface (Fig. 3d–f). The sectional view of the BiSb cathode further confirms that after 150 cycles the BiSb surface is well preserved (Fig. S8). The integrity of cathode structure favors ion and electron transport achieving fast dynamics and long-term cycle stability. In-situ optical photographs of Bi and BiSb cathodes are shown in Fig. 3g–i and Fig. S9 using the optical microscope with a digital camera in transparent batteries. There is no obvious difference between the surface of the Bi cathode before and after electrolyte infiltration, suggesting the grain size of Bi is larger and the number of grain boundary of Bi is smaller as a whole than that of the BiSb (Fig. S9a and Fig. 3g). By comparison, the BiSb cathode shows lots of grain boundaries after electrolyte infiltration as depicted in the inset illustration (Fig. 3h). It is found that the BiSb profiles finer grains yet with more dense grain boundaries than the Bi. Compared to the metal Bi, because the drag effect of Sb solute atoms in the BiSb alloy, Sb atoms will slow down the recrystallization and grain growth rate of the alloy [27]. In this case, the particle size in the steady state of BiSb is much smaller than that of Bi. More grain boundaries not only provide abundant channels to allow ion transport, stabilize the electrode surface, and increase diffusion coefficient, but also improve capacity utilization and create an interconnected 3D network for continuous electron transport [27–29]. During the cycle, the surface of the BiSb cathode is even and stable (Fig. 3i) but the

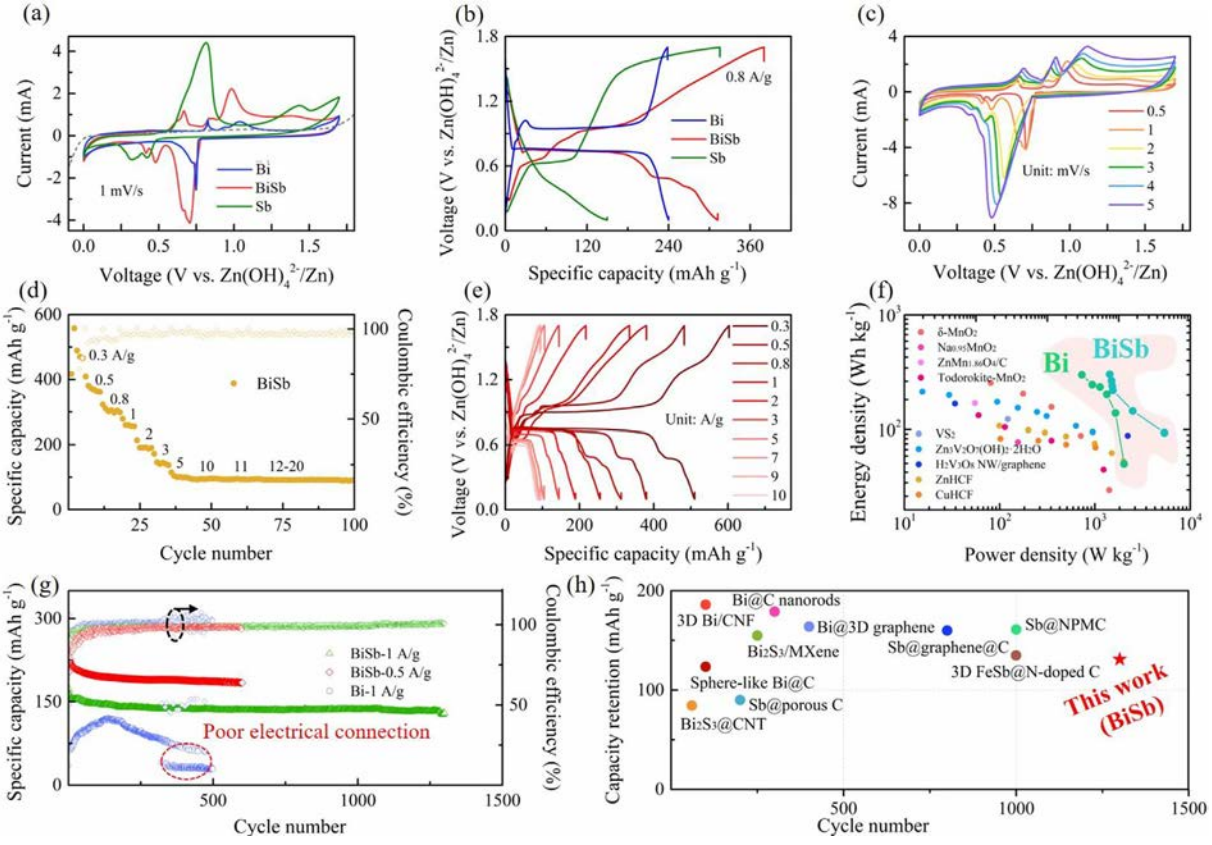

FIGURE 2

Electrochemical properties of BiSb alloy based on the quasi-solid PANa hydrogel electrolyte. (a) CV curves of BiSb, Bi and Sb at 1 mV/s. (b) Galvanostatic charge/discharge (GCD) profiles of BiSb, Bi and Sb at 0.8 A/g. (c) CV curves of BiSb at various scan rates. (d) Rate capability of BiSb. (e) Galvanostatic discharge/charge profiles of BiSb at 0.3–10 Ag^{-1}. (f) Ragone plot of reported aqueous RZBs. Note that the test conditions may be different for different systems here. (g) Cycling performance of Bi and BiSb at 0.5 and 1 Ag^{-1}. (h) The cycling stability of the BiSb cathode compared with other reported Bi-based and Sb-based electrodes.

Bi cathode show protrusions on the surface after 150 cycles, evidencing degradation of the Bi cathode (Fig. S9c).

The difference between BiSb and Bi cathodes in cycling stability is also verified in the electrochemical impedance spectra (EIS) test (Fig. 3j, k, and Table. S1). The faradic impedance, namely the combination of charge-transfer resistance (R_{ct}) and Warburg impedance (Z_W), reflects the kinetics of the battery reactions. All of the EIS plots of BiSb show a semicircle in the high-frequency range and a straight line in the low-frequency region fitted by the equivalent circuit in the inset of Fig. 3k, illustrating a fast ion diffusion and excellent electrical conductivity [30]. The original BiSb (1.26 Ω) has a smaller equivalent series resistance (R_s) including the resistance of the electrolyte and electrode materials than that of Bi (1.7 Ω). The original R_{ct} of BiSb and Bi cathodes are 35 and 13 Ω, respectively (Table S1). The slightly higher R_{ct} of BiSb than bare Bi electrode is due to the Bi_2O_3/SbO_x matrix formed around BiSb. R_{ct} of BiSb decreases to 18 Ω after 200 cycles at first and then slightly increases to 89 Ω after 800 cycles benefiting from the stable BiSb structure during the charge–discharge process. While R_{ct} of Bi firstly decreases to 5.26 Ω after 20 cycles and then sharply rises to 260 Ω after 200 cycles. Initial R_{ct} reduction in both systems is related to the electrochemical polishing of the passivation layer existing on the surface of alloy cathodes [31]. The sharp increment of R_{ct} in the Bi cathode from about 5.26 to 122 Ω after 50 cycles reflects a significant structural degradation of the Bi cathode, which is consistent with previous SEM observations. Z_W is assigned to the $Zn(OH)_4^{2-}$ diffusion in the battery [32]. Generally, the slope is proportional to the Z_W [33]. In the original state, the Warburg tail of both the Bi and BiSb electrodes exhibit a straight line with the angle approaching 45°. As the cycle goes on (Fig. 3j), the angle between the Warburg tail and the Y-axis is less than 45 degrees for BiSb, showing a slower ion diffusion. This is because the diffusion resistance of $Zn(OH)_4^{2-}$ becomes larger during cycling. For the Zn//Bi battery (Fig. 3k), the Z_W of Bi becomes less and less obvious and finally disappears, demonstrating that the ion diffusion is blocked and the reversibility of the electrode is becoming poor.

To gain a better understanding of the reaction mechanism, the phase evolution of the BiSb cathode is studied by the operando XRD technique during the first charge/discharge process at 0.3 Ag^{-1} (Fig. 4a). After firstly discharging to 0.1 V and at the beginning of charging, the peaks at 27.9°, 39°, and 40.8° can be attributed to BiSb, and the peaks at 27.2°, 38°, and 39.7° are indexed to Bi. When charging to 0.5–0.6 V, new peaks at 31.8°, 34.5°, and 36.4° emerge, which can be well assigned to the intermediate phase $BiSbO_4$ (Fig. S10). Further charging, $BiSbO_4$ gradually disappears; instead, the peaks at

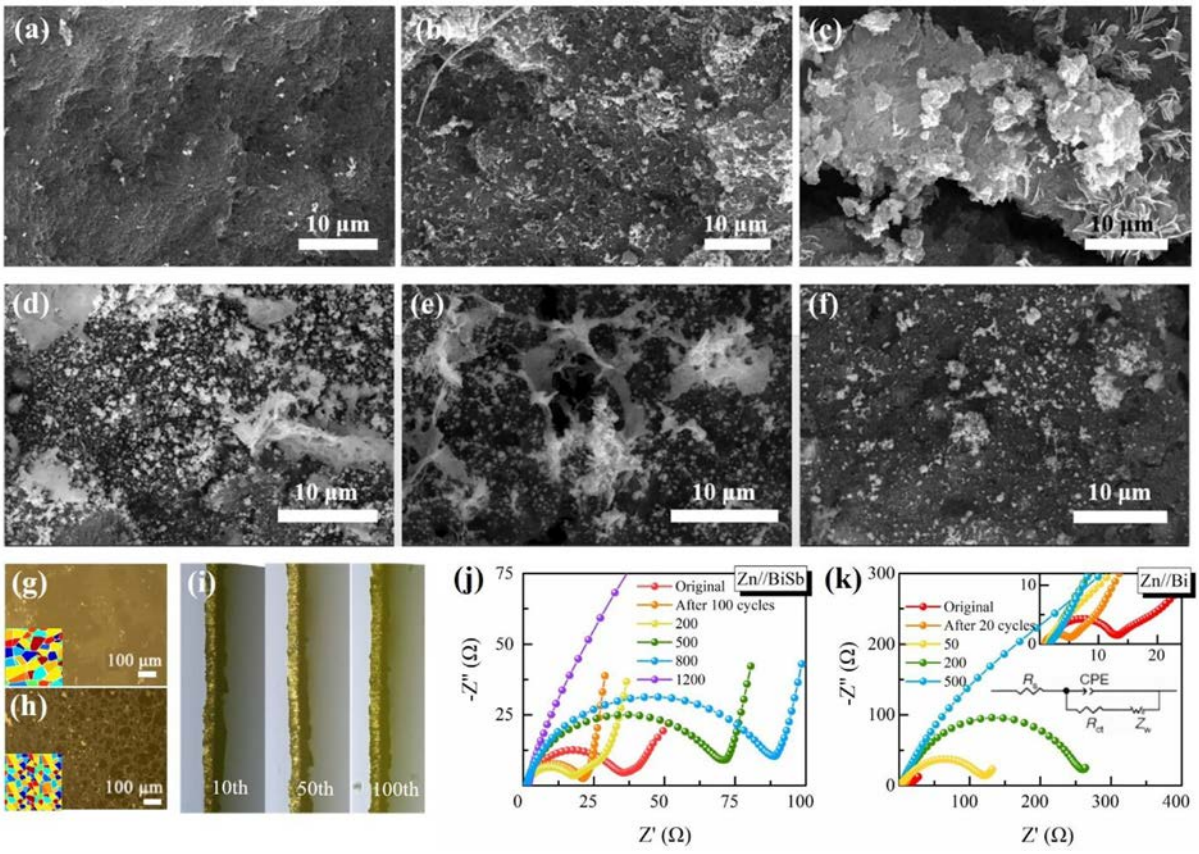

FIGURE 3

Cycling stability and morphological evolution of Bi and BiSb cathodes in 0.3 M $Zn(Ac)_2$ and 6 M KOH aqueous electrolyte at 1 Ag^{-1}. SEM images of the Bi cathode after 50 (a), 100 (b), and 150 (c) cycles. SEM images of the BiSb cathode after 50 (d), 100 (e), and 150 (f) cycles. Optical photographs of Bi (g) and BiSb (h) cathodes in the aqueous electrolyte. In-situ optical microscope images of BiSb cathodes (i) in the Zn//BiSb battery during cycling. EIS analyses of Zn//BiSb (j) and Zn//Bi (k) batteries in the original state and specific cycles.

27.9°, 38.3° and 41.3° indexed to Bi_2O_3 are observed at 0.73 V. There is a phase transition between Bi and Bi_2O_3 accompanying the disappearance of peaks associated with Sb. This is owing to that antimony oxides can dissolve in the strong alkali electrolyte to form SbO_3^- and SbO_2^-. Continuing charging to 1.7 V, only pure Bi_2O_3 phase is identified. In the following discharging, Bi_2O_3 gradually converts to Bi at 0.76 V. As the discharge progresses (0.6–0.5 V (vs. $Zn(OH)_4^{2-}/Zn$)), the SbO_2^- and SbO_3^- in the electrolyte deposite on the cathode and form the intermediate product of $BiSbO_4$. Further discharge, $BiSbO_4$ is finally reduced to the BiSb alloy. To sum up, the BiSb cathode undergoes the reversible conversion-dissolution/deposition reaction of $BiSb \leftrightarrow Bi + SbO_2^- \leftrightarrow Bi + SbO_3^- \leftrightarrow Bi_2O_3$. The electrochemical potentials of the three processes are calculated by the change in Gibbs energy written as [34]:

$$\text{Anode reaction}: Zn(OH)_4^{2-} + 2e^- \leftrightarrow Zn + 4OH^- \quad (1)$$

$$E_1 = E_1^\theta - \left(\frac{0.0592}{2}\right)\log\left(\frac{[OH^-]^4}{[Zn(OH)_4^{2-}]}\right) = -1.295V$$

$$\text{Cathode reaction}: Bi_2O_3 + 3H_2O + 6e^- \leftrightarrow 2Bi + 6OH^- \quad (2)$$

$$E_2 = E_2^\theta - 0.0592\log[OH^-] = -0.5V$$

$$SbO_3^- + H_2O + 2e^- \leftrightarrow SbO_2^- + 2OH^- \quad (3)$$

$$E_4 = E_4^\theta - \left(\frac{0.0592}{2}\right)\log\left(\frac{[OH^-]^2[SbO_2^-]}{[SbO_3^-]}\right) = -0.63V$$

$$SbO_2^- + 2H_2O + 3e^- \leftrightarrow Sb + 4OH^- \quad (4)$$

$$E_3 = E_3^\theta - \left(\frac{0.0592}{3}\right)\log\left(\frac{[OH^-]^4}{[SbO_2^-]}\right) = -0.712V$$

Overall reaction :

$$2BiSb + 3Zn(OH)_4^{2-} \leftrightarrow 2Bi + Sb_2O_3 + 3Zn + 3H_2O + 6OH^- \quad (5)$$

$$\Delta E = E_3 - E_1 = 0.583\ V$$

$$Sb_2O_3 + 2OH^- \leftrightarrow 2SbO_2^- + H_2O \quad (6)$$

$$2SbO_2^- + 3Zn(OH)_4^{2-} \leftrightarrow 3Zn + 2SbO_3^- + 2H_2O + 8OH^- \quad (7)$$

$$\Delta E = E_4 - E_1 = 0.665\ V$$

$$Bi + 3Zn(OH)_4^{2-} \leftrightarrow 3Zn + Bi_2O_3 + 3H_2O + 6OH^- \quad (8)$$

$$\Delta E = E_2 - E_1 = 0.795\ V$$

The calculated results are consistent with the experimental discharge plateaus and reduction peaks of the CV tests. In-situ

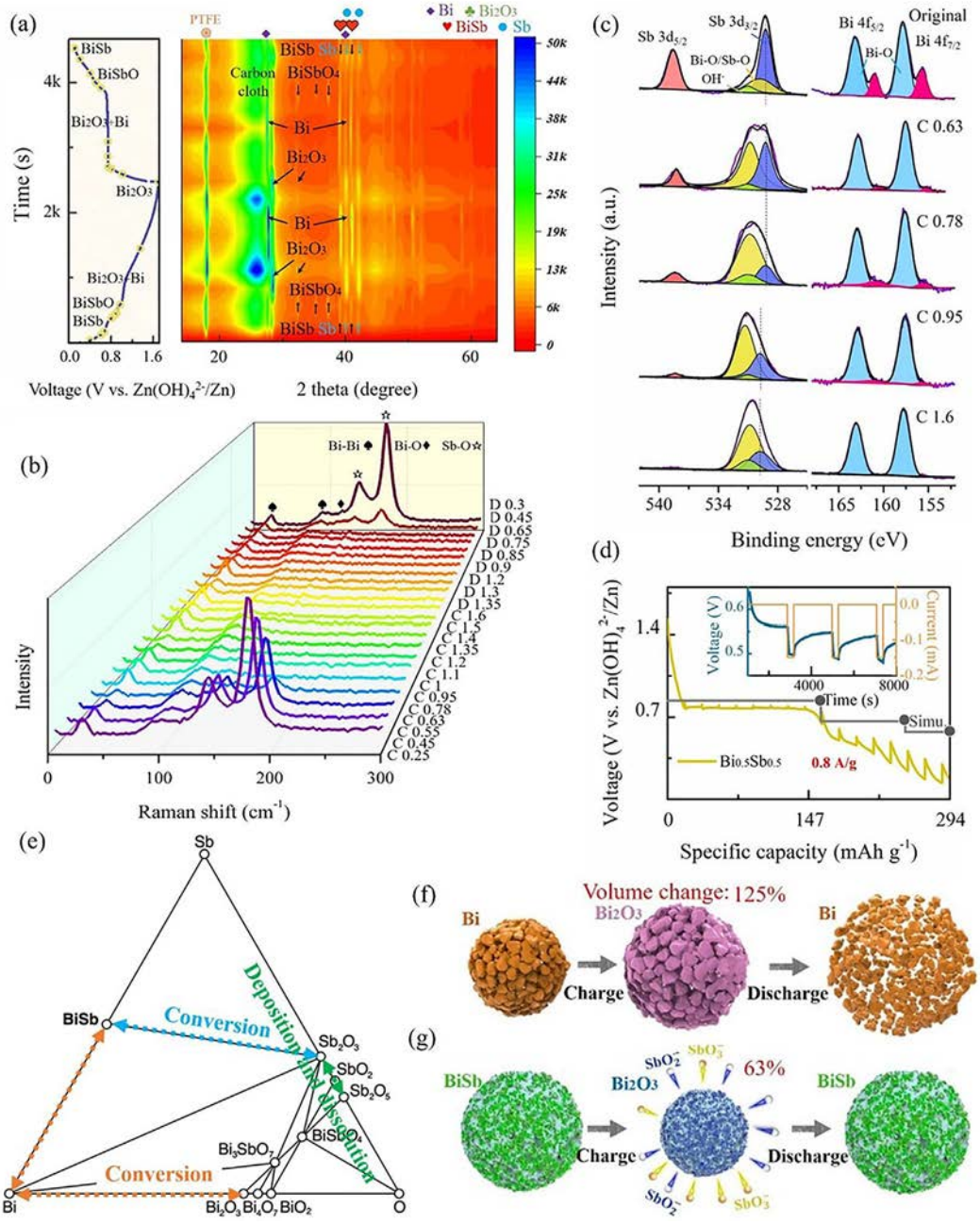

FIGURE 4

Proposed conversion-dissolution/deposition chemistry of Zn//BiSb batteries. (a) Contour plot of the operando XRD results of BiSb cathode during the charge/discharge process with a current density of 0.3 Ag^{-1}. The corresponding charge/discharge curves are shown on the left. (b) In-situ Raman spectra of the BiSb cathode shown at specific charge/discharge states. Specific states charged to 0.25 V and discharged to 0.3 V are abbreviated as C0.25 and D0.3, respectively. (c) Ex-situ high-resolution XPS spectra in the Sb 3d and Bi 4f regions of the BiSb cathode. (d) GITT profiles of BiSb cathode at 0.8 Ag^{-1} with corresponding equilibrium voltages (vs $Zn(OH)_4^{2-}/Zn$) for the conversion reactions from DFT simulations. (e) DFT-calculated Bi-Sb-O phase diagram. Schematic illustrations of morphological evolution of the Bi (f) and BiSb (g) cathodes during the conversion-dissolution/deposition reaction.

Raman spectra are applied to further confirm the evolution of reactants (Fig. 4b and Fig. S11). Peaks ascribed to Sb-O bend-stretch vibrations are found at 140.9 and 177.3 cm^{-1} [35]. Peaks at 97 and 117.9 cm^{-1} are assigned to Bi-Bi and Bi-O vibrations, respectively [36]. When the cathode is charged from 0.25 V to 0.63 V (C 0.25 → C 0.63), the intensity of the peak related to Sb-O vibrations gradually decreases from the highest. The peak disappears while continuing to charge. This phenomenon indicates that trivalent and pentavalent Sb formed during the conversion reactions is gradually dissolved in the strong alkaline electrolyte in the form of SbO_2^- and SbO_3^-. In the discharge phase from D 1.7 to D 0.65, only peaks from Bi-related vibrations are observed at all times. While discharging from 0.45 V to 0.3 V, peaks associated with Sb-O vibrations gradually increase to the highest. It indicates a reversible process of deposition and dissolution. Ex-situ high-resolution XPS spectra for the electrochemi-

cal reaction are depicted in Fig. 4c and Fig. S12. For the original BiSb, the peaks at 538.6 and 529.3 eV are assigned to Sb $3d_{5/2}$ and Sb $3d_{3/2}$, respectively, and the peaks at 531.0 and 529.8 eV correspond to OH^- and Bi-O/Sb-O from O 1 s, respectively; the Bi 4*f* spectrum has peaks at 161 and 155.7 eV referred to Bi $4f_{5/2}$ and Bi $4f_{7/2}$, respectively, whereas peaks shifting to higher energies at 163.2 and 157.9 eV due to the formation of bismuth oxides on the surface [18,37]. During charging from C 0.63 to C 1.6, the proportion of the Bi-O bond (the yellow region on the left and blue region on the right) gradually increases, and the content of Sb decreases, corresponding to the formation of Bi_2O_3 and the dissolution of antimony oxides. During discharging, the content of Bi_2O_3 decreases gradually, and the proportion of Sb increases, as shown in Fig. S12.

The Bi-Sb-O phase diagram is constructed (shown in Fig. 4d) by calculating the lowest energy structure of all known constituents, predicting the thermodynamic phase equilibrium in DFT [38]. The dotted lines in the phase diagram represent the reaction pathways, and the corresponding voltage profiles are calculated in Fig. 4e in agreement with the galvanostatic intermittent titration technique (GITT) voltage profiles at 0.8 A/g. The equilibrium voltages obtained from DFT calculations are also very close to what we calculate via the Gibbs energy [10,39].

Based on the conversion-dissolution/deposition reaction mechanism, we propose the schematic diagrams of Bi and BiSb during the charge/discharge process (Fig. 4f and g). The volume of Bi expands to 125% (Bi → Bi_2O_3) during charging. Then upon discharging, the particles are comminuted seriously (Bi_2O_3 → Bi). After cycles, particle pulverization renders capacity attenuation and poor cycle stability. As for BiSb, during charging, Sb is oxidized to trivalent and pentavalent antimony and slowly dissolves into the electrolyte. Next, Bi is oxidized to Bi_2O_3 and the volume becomes 63% of the original BiSb (BiSb → Bi_2O_3). During discharging, Bi_2O_3 turns to BiSb reversibly. During cycling, the stable BiSb structure endows the Zn//BiSb batteries with enhanced cyclability and high capacity retention. To provide the direct proof of Sb deposition /dissolution into the electrolyte, inductively coupled plasma atomic emission spectrometer (ICP-AES) test of the Zn//BiSb battery with 0.3 M $Zn(Ac)_2$ and 6 M KOH aqueous electrolyte is performed in a beaker (Fig. S13). The reason we don't use polyelectrolyte here is that the gel electrolyte of the disassembled battery is inseparable from the BiSb materials after cycling (Fig. S13a). ICP analyses of dissolved Sb and Bi in the aqueous electrolyte for the third cycle is displayed in Fig. S13d. The initial Sb content in the electrolyte is low. The Sb content gradually increases with discharging to 0.67 V, which corresponds to the dissolution of the electrode material in the alkaline electrolyte. On discharging to below 0.5 V, the amount of dissolved Sb decreases. When the battery continues to discharge to 0.1 V, the content of Sb in the electrolyte reaches the minimum, corresponding to the deposition reaction of Sb. Then, on charging to 0.68 V, the amount of Sb dissolved into the electrolyte increases, and the content of Sb further rises with charging to 0.97 V, which corresponds to the dissolution of the Sb from the cathode to the alkaline electrolyte. Continuing to charge to 1.7 V, the Sb content in the electrolyte returns to a high point. The content of Bi does not change significantly during discharge and charging. This phenomenon can reflect in part the deposition/dissolution mechanism of Sb in the polyelectrolyte. Given the dissolution/deposition mechanism, Sb loss during cycling is further analyzed in the beaker battery mentioned above (Fig. S13e). The concentration of Sb in the aqueous electrolyte rapid increases in the initial cycles and becomes stable after 150 cycles. Compared to the concentration of Bi in the aqueous electrolyte, we speculate that there is Se loss in the beaker battery. Although we can't detect the specific loss of Sb with PANa gel electrolyte, we predicate that Sb loss would be inhibited due to the water-locking effect of the gel electrolyte. To further alleviate the loss of Sb during cycle, strategies like adding a small amount of Sb to the alkaline electrolyte (0.3 M $Zn(Ac)_2$ and 6 M KOH) in advance, and then immersing PANa hydrogel in the electrolyte containing SbO_2^- may work. Also, it should be noted that the Bi_2O_3/SbO_x matrix formed around BiSb also takes part in the reaction of storing $Zn(OH)_4^{2-}$ in the high concentration polyelectrolyte following the equations (6)-(8). Amorphous nature of the matrix provides buffering effect on the strain generated by multiple phase transition. Conductive nature of the matrix ensures BiSb nanoparticles tightly bonded with carbon and improves the structure stability greatly [24]. The Bi_2O_3/SbO_x matrix not only improves the conductivity of the electrode, but also inhibit the overgrowth and aggregation of BiSb grains [40], and releases the volume change of BiSb by providing ample elastic space.

It should be noted that, BiSb, as an alloy cathode, has lower resistance at a lower temperature (a property of metal). This is different from many metal-oxide semiconductor-based cathode materials (higher resistance at a lower temperature). The decreased resistance of the alloy electrode is believed to benefit the performance of a battery at low temperatures. We further assess the low-temperature electrochemical properties of the prepared BiSb cathode in RZBs. The electrical properties of the BiSb and Bi samples are firstly studied at different temperatures. Current-voltage (I-V) plots in Fig. 5a and Fig. S14 show the change of conductivity of BiSb and Bi with temperature (25 to −195 °C) by electrical transport measurements, respectively. As expected, the resistance of BiSb decreases with decreasing temperatures. The linear relationships of I-V manifest the ohmically conductive contacts between Au electrodes and the BiSb nanoparticle. The subsequent temperature-dependent current of the BiSb and Bi devices at 0.1 V is displayed in Fig. 5b. When the temperature drops from 25 to −90 °C, the currents of the BiSb and Bi nanoparticles sharply rise, suggesting a rapid reduction of the resistance (the yellow region in Fig. 5b). Also, the current of the BiSb device is 1.59 times higher than that of Bi indicating that the introduction of Sb in metal Bi potentially enhances its conductivity [20]. Fig. 5c shows the rate capability at different temperatures, in which Zn//BiSb exhibits the best capacities at 40 °C. It delivers capacities of 262, 226, 198, 164, 161, 152, 142, 134, 125 and 116 mAh g^{-1} at 1.5, 2, 2.5, 3, 3.5, 4, 4.5, 5, 5.5 and 6 Ag^{-1}, respectively. The corresponding GCD profiles at various temperatures and 1 Ag^{-1} are shown in Fig. S15. Even at temperatures as low as −10 and −20 °C, there are still 210 and 197 mAh g^{-1} reserved at 1 Ag^{-1}, respectively, indicating a high tolerance of conversion-dissolution/deposition reaction of the BiSb cathode to the extreme-temperature. Fig. 5d summarizes capacity retention ratio of Zn//BiSb batteries at vari-

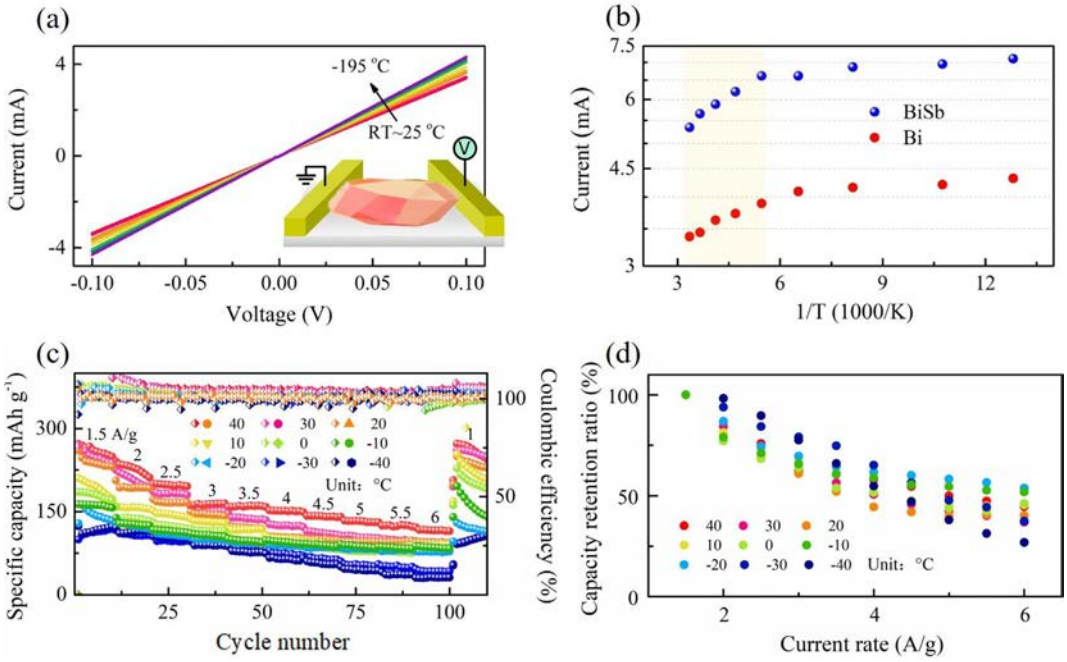

FIGURE 5

Low temperature performance of Zn//BiSb batteries. (a) I-V curves at various temperatures of BiSb with a schematic illustration of the assembled BiSb device for the electrical transport test as inset. (b) The temperature-dependent current analyses on the Bi and BiSb devices at 0.1 V. (c) Rate capability of the Zn//BiSb batteries from −40 to 40 °C. (d) Comparison of capacity retention of Zn//BiSb batteries at various temperatures and current rates. Here the capacity retention ratio is calculated by $\left(\frac{\text{discharge capacity at different rates at a selected temperature}}{\text{discharge capacity at 1.5 A/g at a selected temperature}} \times 100\%\right)$.

ous temperatures and current rates compared to the corresponding discharge capacities at 1.5 Ag^{-1}. Even at −20 °C the capacity retentions at 2–6 Ag^{-1} remain 54–87%. In stark contrast, the Bi cathode shows capacity retentions of only 86 and 63 mAh g^{-1} at −10 and −20 °C at 1 Ag^{-1} due to lower conductivity and degraded surface of the Bi cathode than that of BiSb, respectively, and the limited circulation of 40 cycles at 40 °C due to severe side reactions including H_2/O_2 evolution reactions, and huge volume expansion of Bi cathode (Fig. S16). The phenomena indicate relatively low conductivity, poor structure stability, and phase transition greatly affected by temperature for the Bi cathode. The low-temperature cyclability of Zn//BiSb is shown in Fig. S17. The battery maintains 82 mAh g^{-1} after 640 cycles even at −20 °C and 1 Ag^{-1}. Additionally, the excellent performance of Zn//BiSb cells encourages us to further assemble pouch batteries in the air. The open-circuit voltage (OCV) of the soft-package two batteries in series can reach 2.11 V (Fig. S18). The pouch-type Zn//BiSb battery with the polyelectrolyte delivers a capacity of 3.89 mAh after 250 cycles (Figure. S19a), and a high CEs (above 96%) are achieved after 15 cycles (Figure. S19b), further demonstrating the practicability of our Zn//BiSb battery.

Conclusion

In summary, we demonstrate a high-performance aqueous Zn//BiSb battery based on high-concentrated strong-basic polyelectrolyte. We elucidate a unique conversion-dissolution/deposition electrochemical mechanism (BiSb $\leftrightarrow Bi + SbO_2^- \leftrightarrow Bi + SbO_3^- \leftrightarrow Bi_2O_3$) through in situ XRD, Raman, ex-situ XPS tests, and DFT calculations. The three-step transition reactions at 0.795, 0.665, and 0.583 V correspond to three pairs of redox peaks in CV curves. Amorphous oxide layer SbO_x and Bi_2O_3 formed around BiSb during the mechanical milling process, and fine grains of BiSb with dense grain boundary effectively maintain the electrode integrity. Unique reaction mechanism, stable structure, and excellent electrical conductivity combined with high concentration polyelectrolyte enable an excellent electrochemical performance. The BiSb cathode shows a large capacity of 512 mAh g^{-1} at 0.3 Ag^{-1} and excellent rate capability of 90 mAh g^{-1} even at 20 Ag^{-1}, and cycling stability with a capacity retention of 130 mAh g^{-1} after 1300 cycles at 1 Ag^{-1}. Notably, even at a temperature as low as −20 °C, there is 197 mAh g^{-1} reserved at 1 Ag^{-1}. In contrast, metal Bi exhibit limited performance, emphasizing the structure buffering effects in the alloy structure. In comparison with other reported RZBs, Zn//BiSb exhibits high specific energy (303 Wh kg^{-1}_{BiSb} at 0.3 Ag^{-1}). Our research reveals that metal electrode can provide a large capacity for Zn batteries through a conversion-dissolution/deposition mechanism and alloying is an effective approach to develop stable metal electrodes by structural buffering.

CRediT authorship contribution statement

Yuwei Zhao: Conceptualization, Methodology, Writing. **Feng Jiang:** Methodology. **Hu Hong:** Methodology. **Donghong Wang:** Methodology. **Qing Li:** Methodology. **You Meng:** Methodology. **Zhaodong Huang:** Methodology. **Ying Guo:** Methodology. **Xinliang Li:** Methodology. **Ao Chen:** Methodology. **Rong Zhang:** Methodology. **Shaoce**

Zhang: Methodology. **Johnny C. Ho:** Methodology. **Zhenpeng Yao:** Conceptualization, Funding acquisition, Writing – review & editing. **Weishu Liu:** Conceptualization, Funding acquisition, Writing – review & editing. **Chunyi Zhi:** Conceptualization, Funding acquisition, Writing – review & editing.

Declaration of Competing Interest

The authors declare that they have no known competing financial interests or personal relationships that could have appeared to influence the work reported in this paper.

Acknowledgements

This research was supported by the National Key R&D Program of China under Project 2019YFA0705104. The work was also partially sponsored by GRFs under Project CityU 11305218, CityU 11212920, the Guangdong Innovative and Entrepreneurial Research Team Program (the Grant No. 2016ZT06G587), and the Shenzhen Sci-Tech Fund No. KYTDPT20181011104007. Z.Y. was supported by the US Department of Energy, Office of Science - Chicago under Award Number DE-SC0019300.

Appendix A. Supplementary data

Supplementary data to this article can be found online at https://doi.org/10.1016/j.mattod.2021.09.023.

References

[1] Y. Cheng et al., Adv. Funct. Mater. (2020) 30.
[2] L. Ma et al., Nature Energy 5 (2020) 743;
L.E. Blanc, D. Kundu, L.F. Nazar, Joule 4 (2020) 771;
J. Huang et al., Small Methods (2019) 3.
[3] D. Li et al., Angew. Chem. Int. Ed. Engl. (2021).
[4] J. Zheng et al., Energy Environ. Sci. 12 (2019) 615.
[5] L. Zhang et al., Adv. Energy Mater. (2015) 5.
[6] P. Hu et al., Nano Lett 18 (2018) 1758;
H.L. Pan et al., Nature Energy 1 (2016) 1;
N. Zhang et al., Nat Commun 8 (2017) 405.
[7] C. Han et al., J. Mater. Chem. A 8 (2020) 15479.
[8] Z. Huang et al., Adv. Energy Mater. (2020) 10.
[9] C. Yang et al., Nature 569 (2019) 245.
[10] D. Wang et al., Nano Energy (2020) 71.
[11] X. Lu et al., Chem. Mater. 28 (2016) 1236.
[12] K. Huang et al., J. Mater. Chem. A 6 (2018) 434.
[13] K. Lei et al., Angew. Chem. Int. Ed. Engl. 57 (2018) 4687.
[14] J. Song et al., Nanoscale 11 (2018) 348.
[15] W. Ye et al., Adv. Energy Mater. (2020) 10;
H. Gao et al., ACS Nano 12 (2018) 3568.
[16] N. Wang et al., Adv. Mater. 28 (2016) 4126.
[17] X. Ge et al., Angew. Chem. 131 (2019) 14720.
[18] P. Xiong et al., ACS Nano 14 (2020) 1018.
[19] Q. Li et al., Adv. Energy Mater. (2021).
[20] H. Tan et al., Adv. Funct. Mater. (2019) 29.
[21] Y. Zhao, A. Manthiram, Chem. Mater. 27 (2015) 3096.
[22] J. He et al., Mater. Chem. Front. 2 (2018) 437.
[23] D. Aurbach, J. Power Sources 89 (2000) 206;
J. Chen et al., Nat. Energy 5 (2020) 386.
[24] Z. Wang et al., J. Colloid Interface Sci. 580 (2020) 429.
[25] C. Xu et al., Angew. Chem. Int. Ed. Engl. 51 (2012) 933;
M.H. Alfaruqi et al., Electrochem. Commun. 60 (2015) 121;
R. Trocoli, F. La Mantia, ChemSusChem 8 (2015) 481;
P. He et al., Adv. Energy Mater. 7 (2017) 1601920;
D. Kundu et al., Nat. Energy 1 (2016) 1;
B. Zhang et al., Chem. Commun. 50 (2014) 1209;
Q. Pang et al., Adv. Energy Mater. 8 (2018) 1800144;
J. Lee et al., Electrochim. Acta 112 (2013) 138;
D. Wang et al., Energy Storage Mater. 36 (2021) 272.
[26] F. Yang et al., Chem. - Eur. J. 22 (2016) 2333;
X. Cheng et al., J. Mater. Chem. A 7 (2019) 4913;
Y. Jin et al., Nanoscale 9 (2017) 13298;
Q. Yang et al., New J. Chem. 44 (2020) 3072;
Y. Zhao et al., Adv. Sci. (Weinh) 8 (2020) 2002590.
[27] C. Wang et al., Chem. Mater. 27 (2015) 5647–5656.
[28] S. Han et al., J. Power Sources 240 (2013) 155–167.
[29] H.-K. Tian, R. Jalem, Y. Tateyama, J. Mater. Chem. A 9 (2021) 15207–15216.
[30] Y. Zhao et al., ACS Nano 13 (2019) 7270.
[31] P. Senguttuvan et al., Adv. Energy Mater. (2016) 6.
[32] M. Mohamedi et al., Electrochim. Acta 48 (2002) 79–84.
[33] E. Warburg, Ann. Phys. 303 (1899) 493–499.
[34] C.-X. Zu, H. Li, Energy Environ. Sci. (2011) 4.
[35] N. Li et al., J. Mater. Chem. A 3 (2015) 5820.
[36] A. Wang et al., Small 16 (2020) e2004022.
[37] D. Kong et al., Chem. Commun. 51 (2015) 2798.
[38] A. Belsky et al., Acta Crystallogr., Sect. B: Struct.. Crystallogr. Cryst. Chem. 58 (2002) 364;
G. Liang et al., Nat. Rev. Mater. 6 (2020) 109.
[39] Y. Guo et al., Energy Environ. Sci. 13 (2020) 2888;
S. Yang et al., Energy Storage Mater. 33 (2020) 230.
[40] P.K. Allan et al., J. Am. Chem. Soc. 138 (2016) 2352–2365.